

Information Filtering via Variational Regularization for Robot Manipulation

Jinhao Zhang * Wenlong Xia * Yaojia Wang Zhexuan Zhou Huihe Li Yichen Lai Haoming Song
Youmin Gong Jie Mei✉

Abstract

Diffusion-based visuomotor policies built on 3D visual representations have achieved strong performance in learning complex robotic skills. However, most existing methods employ an oversized denoising decoder. While increasing model capacity can improve denoising, empirical evidence suggests that it also introduces redundancy and noise in intermediate feature blocks. Crucially, we find that randomly masking backbone features at inference time (without changing training) can improve performance, confirming the presence of task-irrelevant noise in intermediate features. To this end, we propose Variational Regularization (VR), a lightweight module that imposes a timestep-conditioned Gaussian over backbone features and applies a KL-divergence regularizer, forming an adaptive information bottleneck. Extensive experiments on three simulation benchmarks (RoboTwin2.0, Adroit, and MetaWorld) show that, compared to the baseline DP3, our approach improves the success rate by 6.1% on RoboTwin2.0 and by 4.1% on Adroit and MetaWorld, achieving new state-of-the-art results. Real-world experiments further demonstrate that our method performs well in practical deployments. Code will released.

1. Introduction

Imitation learning (learning from demonstrations) is a practical workhorse for robot manipulation: it avoids reward engineering and can directly leverage expert data (Osa et al., 2018; Argall et al., 2009). However, manipulation is contact-rich and often multimodal, and pure behavior cloning can be brittle under distribution shift (Ross et al., 2011).

Recently, diffusion-based visuomotor policies have emerged as a powerful class of generative policies for robot manipulation, modeling action sequences as samples from a

* Correspondence to: Jie Mei <jmei@hit.edu.cn>, Jinhao Zhang <jinhaozhang0705@gmail.com>.

conditional denoising process. Early diffusion-based policies condition primarily on RGB observations (together with proprioception), which is convenient and scalable (Chi et al., 2023; Wang et al., 2024; Prasad et al., 2024), but may under-specify 3D geometry and contacts that are crucial for contact-rich manipulation. To better capture geometry, recent work has begun to incorporate 3D visual representations (e.g., robot-centric point clouds) as policy conditioning, leading to stronger generalization and performance on challenging manipulation tasks (Ze et al., 2024; Cao et al., 2024; Zhang et al., 2025; Xia et al., 2025).

Our work builds on the current state-of-the-art 3D diffusion-based policy DP3 (Ze et al., 2024), whose point-cloud encoder is intentionally simple yet produces a compact and information-rich scene representation. Interestingly, this compact conditioning signal (a single 64-dimensional vector) is typically paired with a large U-Net denoising decoder (~250M parameters) whose intermediate feature blocks are extremely wide (2048×4)—a design inherited from diffusion models for image generation (Ho et al., 2020). This encoder–decoder asymmetry suggests that the decoder may introduce redundancy and task-irrelevant noise into its intermediate representations. Yet the decoder is often treated as a black box, and the role of its internal representations for manipulation decision making remains under-explored.

In this paper, we show that intermediate backbone features in such large decoders can be redundant and noisy for manipulation tasks: surprisingly, a simple masking of backbone features at inference time can improve success rates on several tasks (even when entire blocks are masked out), indicating that they may contain task-irrelevant noise. Motivated by this observation, we propose **Variational Regularization (VR)**, a lightweight module that imposes a timestep-conditioned variational bottleneck on backbone features and regularizes it with a KL term for adaptive information filtering. We provide a principled justification via the variational information bottleneck framework (Tishby & Zaslavsky, 2015; Alemi et al., 2016), and demonstrate consistent gains on three simulation benchmarks: RoboTwin2.0 (Chen et al., 2025), Adroit (Rajeswaran et al., 2017), and MetaWorld (Yu et al., 2020). In summary, our main contributions are as follows:

- We conduct a targeted investigation of internal U-Net

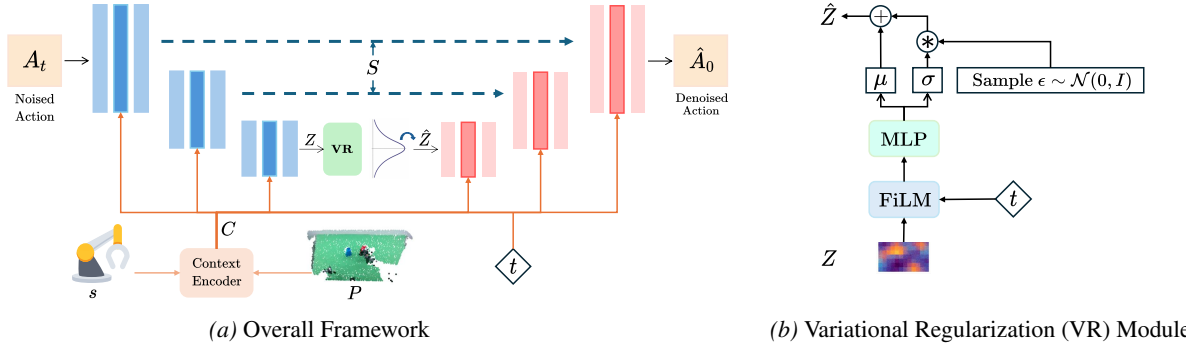


Figure 1. Our proposed method, Variational Regularization (VR), adaptively filters out noise and redundant information from features. (a) Our method, built on DP3, introduces a Variational Regularization module immediately after the last downsampling features in the U-Net decoder, where noise is most likely to accumulate, enabling effective information filtering. (b) Architecture of the Variational Regularization module: it modulates the features conditioned on the diffusion timestep, then predicts the feature-wise mean and standard deviation, and uses the reparameterization trick to obtain the filtered features.

decoder representations in diffusion-based manipulation policies, revealing redundancy and noise in backbone features via inference-time masking.

- We propose **VR**, a simple timestep-conditioned variational bottleneck that adaptively filters intermediate features with negligible computational overhead. We also provide an information-bottleneck interpretation and theoretical guarantees that connect our objective to a variational evidence lower bound (ELBO).
- We demonstrate that our method, **VR**, consistently improves the baseline model’s performance on RoboTwin 2.0, Adroit, and MetaWorld, achieving state-of-the-art average success rates. Real-world experiments further show that VR performs well in practical deployments.

2. Related Work

2.1. Diffusion Models for Robotic Manipulation

Diffusion models were initially popularized for high-fidelity image synthesis (Ho et al., 2020; Song et al., 2020a;b; Rombach et al., 2022). In robotic manipulation, diffusion-based policies have demonstrated strong robustness and multimodality, achieving high performance across diverse manipulation skills (Xian et al., 2023; Liu et al., 2024; Yan et al., 2025). Diffusion Policy (Chi et al., 2023) is the first to establish the paradigm of representing a manipulation policy as a conditional diffusion process over action sequences. DP3 incorporates 3D geometric conditioning via compact point-cloud representations to improve fine-grained, contact-rich manipulation generalization (Ze et al., 2024); Mamba Policy adopts selective state-space modeling to enhance efficiency and deployability while retaining strong manipulation performance (Cao et al., 2024); ISS Policy introduces implicit scene supervision during training to strengthen geometric consistency without adding inference-time overhead (Xia et al., 2025).

2.2. Variational Information Bottleneck

The information bottleneck (IB) provides an information-theoretic characterization of representation learning as a trade-off between prediction and compression. Tishby & Zaslavsky (2015) first advocated information-theoretic objectives for deep neural networks; however, directly optimizing the IB objective does not scale well to deep architectures. Consequently, Chalk et al. (2016) and Achille & Soatto (2018) derived IB-related variational objectives in the contexts of sparse coding and variational dropout/disentangled representations, respectively. Deep Variational Information Bottleneck (VIB) (Alemi et al., 2016) introduces variational approximations to the decoder $p(y | z)$ and the latent prior $p(z)$, thereby instantiating an information-compressive regularization principle for supervised learning. Empirically, VIB can improve both generalization and the adversarial robustness.

In robot manipulation, Bai et al. (2025) were among the first to explore the application of the information bottleneck (IB) principle, applying it to the scene encoder to facilitate multimodal fusion. In contrast, we do not aim to improve the scene representation; instead, we impose the bottleneck on the decoder side to filter redundant information in the intermediate representation. Moreover, we adopt the variational information bottleneck (VIB) in place of IB, which eliminates the need to train a separate discriminator to estimate mutual information, making our approach simpler and more efficient.

3. Preliminaries

3.1. Diffusion Models

Denoising Diffusion Probabilistic Models (Ho et al., 2020) (DDPM) learn to generate clean data by reversing a simple forward noising process. In the forward diffusion, Gaussian

noise is added step-by-step to form a Markov chain:

$$q(x_t | x_{t-1}) = \mathcal{N}\left(x_t; \sqrt{1 - \beta_t} x_{t-1}, \beta_t I\right) \quad (1)$$

which gradually transforms data into a standard Gaussian. This process also admits a closed-form for sampling an intermediate state $q(x_t | x_0) = \mathcal{N}(x_t; \sqrt{\bar{\alpha}_t} x_0, (1 - \bar{\alpha}_t)I)$, where $\alpha_t = 1 - \beta_t$ and $\bar{\alpha}_t = \prod_{s=1}^t \alpha_s$.

Starting from $x_T \sim \mathcal{N}(0, I)$, the reverse denoising process is modeled with a parameterized Gaussian $p_\theta(x_{t-1} | x_t) = \mathcal{N}(x_{t-1}; \mu_\theta(x_t, t), \Sigma_\theta(x_t, t))$. In practice, a neural network $\epsilon_\theta(x_t, t)$ is trained to predict the injected noise, yielding the standard mean-squared error objective:

$$\mathcal{L} = \mathbb{E}_{t, x_0, \epsilon} \left[\|\epsilon - \epsilon_\theta(\sqrt{\bar{\alpha}_t} x_0 + \sqrt{1 - \bar{\alpha}_t} \epsilon, t)\|_2^2 \right] \quad (2)$$

which can be interpreted as a variational bound on the negative log-likelihood. In this work, we adopt the DDPM framework and use DDIM-style (Song et al., 2020a) sampling to enable efficient, high-quality generation within our policy architecture.

3.2. Problem Formulation

Given a set of expert demonstrations consisting of complex robot-skill trajectories, our goal is to learn a visuomotor policy π that maps visual observations to actions. Concretely, we use single-view, robot-centric point clouds P together with proprioceptive states s as the denoising condition C , and predict an H -step future action trajectory A_0 , so that the robot can not only reproduce the demonstrated skill but also generalize beyond the training data.

4. Methodology

4.1. Overview

As shown in Fig. 1a, we adopt the current state-of-the-art 3D visuomotor diffusion-based policy, the 3D Diffusion Policy (Ze et al., 2024), as our backbone. It employs a simple yet effective point-cloud encoder to map the input point cloud into a compact representation as scene context, and then conditions a 1D U-Net (Ronneberger et al., 2015) to predict the original action \hat{A}_0 from the noisy action input $A_t \sim q(A_t | A_0)$ (Ramesh et al., 2022). In this architecture, the U-Net decoder first downsamples the input into a high-channel feature space (e.g., in the original DP3 implementation, from 16×14 to 2048×4), and then progressively upsamples it back to the original trajectory space. The larger intermediate feature blocks increase model capacity and typically improve denoising performance (Dhariwal & Nichol, 2021; Nichol & Dhariwal, 2021), but they may also induce noisy responses (Oktay et al., 2018).

In this work, we argue that, given the compact scene context produced by the point-cloud encoder, *excessively wide inter-*

mediate feature blocks might be redundant and can lead to noisy responses. Motivated by this insight, we first conduct targeted experiments to quantify the noise and redundancy in intermediate features, thereby validating our hypothesis. We then propose a simple and effective remedy: applying a variational information regularization to “filter out” task-irrelevant information. Our experiments demonstrate that this plug-and-play approach learns more meaningful intermediate representations with almost no additional model parameters, leading to consistent improvements in final performance.

4.2. Noisiness of Backbone Features in U-Net

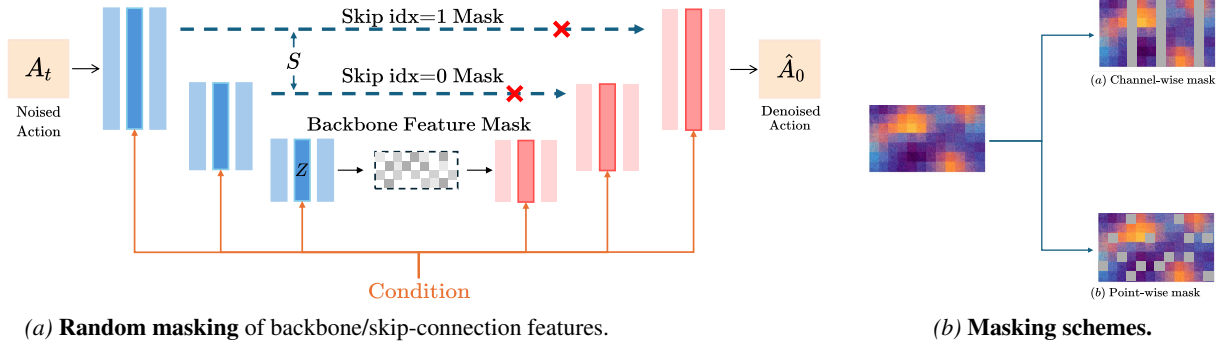
To further probe our insight, we conduct a quantitative analysis of the functional roles and structural properties of different components in the DP3 (Ze et al., 2024) U-Net decoder across several tasks from Adroit and MetaWorld. Specifically, following FreeU (Si et al., 2024), we partition U-Net features into two groups: backbone features Z and skip-connection features S . Unlike FreeU, however, we treat the feature produced by the final downsampling stage as the backbone feature, since it serves as the source of all subsequent upsampled features, directly analyzing this feature simplifies the experimental pipeline without sacrificing the reliability of the results.

As shown in Fig. 2a, given a trained model, we perform random feature masking at test time with probability p and measure the resulting change in task performance, which serves as a proxy for the contribution of the masked features to decision making (Li et al., 2016). To further investigate the information structure within the backbone features, we apply two masking schemes illustrated in Fig. 2b—point-wise masking and channel-wise masking—and examine whether they lead to significantly different performance changes.

For each experiment, we evaluate **100 random seeds** (0–99), and for each seed we run **100 test rollouts** (10,000 rollouts in total). We report the mean success rate to reduce the effect of statistical noise. The results are shown in Fig. 3. We summarize the key conclusions as follows.

Backbone features tend to contain noise of unquantified magnitude. To distill general patterns from our experimental results, we focus on two metrics:

1. **Peak performance under different masking probabilities vs. no masking.** If the best performance achieved with masking exceeds the no-masking baseline, it suggests that the features are **redundant and/or noisy**. In this case, appropriately masking these noisy structures can act as a form of regularization and **improve performance**.



(a) Random masking of backbone/skip-connection features.

(b) Masking schemes.

Figure 2. Random masking analysis of U-Net decoder intermediate features. (a) We apply masks separately to the backbone features and to skip connections at different decoder depths to study the role of each component. (b) We consider two masking schemes—point-wise mask and channel-wise mask—to probe how information is organized within the representations and whether intermediate features contain redundant or noisy signals.

2. **Performance change when masking the entire feature block vs. no masking.** Comparing the model’s performance after removing the whole backbone feature block to the no-masking baseline provides a rough proxy for the feature’s **signal-to-noise ratio**. If performance **improves**, the block likely contains more noise than useful signal; if performance **degrades**, the block likely contributes more beneficial information.

As indicated by the purple curve in Fig. 3a–3h, simply masking the backbone features at *test time* consistently yields a higher peak performance (though the peak is achieved at different masking probabilities p). This clearly indicates that backbone features may contain task-irrelevant noisy responses or redundant information. However, the amount of noise in the backbone features varies across tasks. For Adroit-Door, Adroit-Pen, and MetaWorld-Disassemble, masking the entire backbone feature block improves performance, indicating a net negative contribution (more noise than signal). In contrast, for MetaWorld-StickPull, dropping the backbone features degrades performance, suggesting that they still provide decision-relevant signal. Overall, in most manipulation tasks, *the U-Net decoder’s backbone features are likely noisy and redundant, yet they can also contain decision-relevant signal; their signal-to-noise ratio varies across tasks.*

Backbone features exhibit no clear information organization, or their organization is highly complex. As shown in Fig. 3a–3h, the performance trends under the two masking schemes (channel-wise and point-wise) are broadly similar (with or without VR). This suggests that the backbone features are organized in a complex, highly coupled manner, rather than storing different aspects of information in a simple per-point or per-channel fashion.

The effect of deeper skip connections is not significant. As shown in Fig. 2, the U-Net employed by DP3 comprises three down/up-sampling stages. We conduct an analogous

analysis on its two skip connections, with results illustrated in Fig. 3i–3l. We observe that masking the shallow skip connection (idx=1) consistently degrades performance, whereas masking the deeper one (idx=0) has a smaller and less consistent effect. In particular, its impact is not significant and appears task-dependent.

Based on the above three observations, we identify the central tension: during downsampling, the U-Net decoder’s backbone features become contaminated with noise, and their signal-to-noise ratio is task-dependent. Given the complexity/unstructured nature of how information is organized in these features, we require a mechanism that can *adaptively filter out task-irrelevant information while, to some extent, suppressing irrelevant noise*.

4.3. Information Filtering by Variational Regularization

As shown in Fig. 1a, to address the challenges summarized in Section 4.2, we introduce a variational regularization module after the last downsampling stage. This module adaptively extracts task-relevant information while suppressing noise in the backbone features Z .

Formally, our goal is to distill from Z a representation \hat{Z} with a higher signal-to-noise ratio. Following Alemi et al. (2016), we parameterize \hat{Z} by a conditional distribution. Moreover, since the noise level of the model inputs varies across diffusion timesteps, the amount and structure of noise in Z may also change accordingly. We therefore incorporate the diffusion timestep t into the regularization module as an additional conditioning signal, yielding $\hat{Z} \sim p_\theta(\cdot | Z, t)$. In particular, we choose this distribution to be Gaussian:

$$p_\theta(\hat{Z} | Z, t) = \mathcal{N}(\mu_\theta(Z, t), \sigma_\theta^2(Z, t)). \quad (3)$$

We then feed \hat{Z} into the subsequent upsampling blocks of the U-Net to obtain the final denoised prediction \hat{A}_0 . Here, we adopt x_0 -*prediction* (i.e., predicting the clean sample x_0). During training, we regularize p_θ to encourage it to

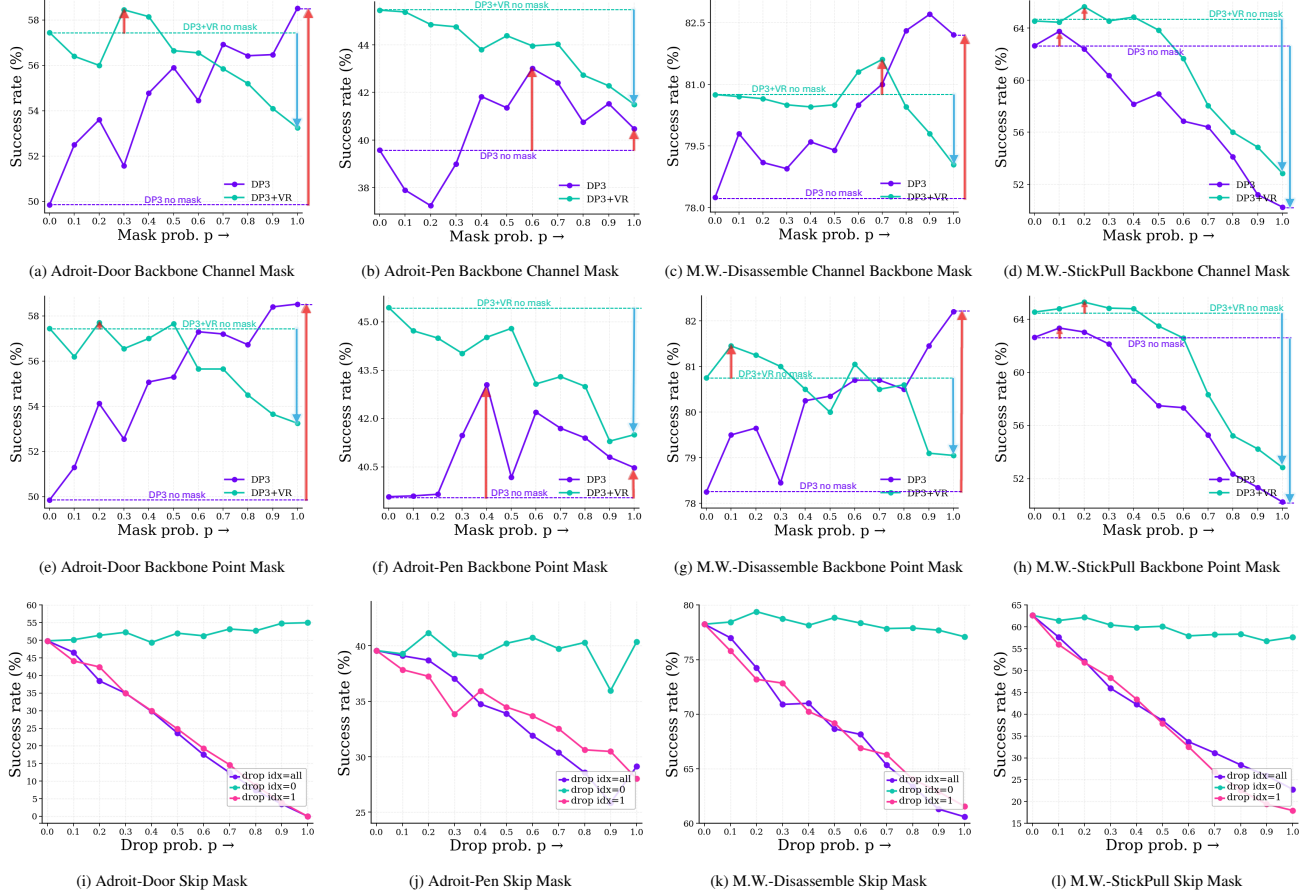


Figure 3. Noisiness analysis of U-Net decoder features on Adroit-Door, Adroit-Pen, MetaWorld Disassemble, and MetaWorld StickPull, where M.W. denotes an abbreviation for MetaWorld. (a–d) Channel-wise masking of backbone features; (e–h) point-wise masking of backbone features. Backbone features are likely noisy and redundant, yet they can also contain decision-relevant signal. Our variational regularization (VR) module substantially improves the signal-to-noise ratio of the backbone features. (i–l) Skip-connection feature mask applied to different skip depth (drop_idx).

match a standard normal distribution q . Consequently, after introducing the regularization module, the overall loss can be expressed as the sum of the denoising loss and an additional regularization term:

$$\mathcal{L}_{\text{policy}} = \mathbb{E} \left[\|\hat{A}_0 - A_0\|^2 + \beta \text{KL}(p_\theta(\hat{Z}|Z, t) \| q(\hat{Z})) \right] \quad (4)$$

Here, β controls the strength of the regularization. Intuitively, the denoising objective encourages \hat{Z} to extract task-relevant information from Z , while the regularizer acts as an information bottleneck that filters out redundant content, thereby pushing \hat{Z} to retain only the most decision-critical signals from Z .

As illustrated in Fig. 1b, during implementation we first inject the timestep t into the feature Z via a FiLM layer (Perez et al., 2018). We then use two separate MLPs to predict the mean $\mu_\theta(Z, t)$ and standard deviation $\sigma_\theta(Z, t)$ of \hat{Z} , and finally obtain \hat{Z} by the reparameterization trick (Kingma & Welling, 2013):

$$\hat{Z} = \mu_\theta(Z, t) + \sigma_\theta(Z, t) \odot \epsilon, \quad \epsilon \sim \mathcal{N}(\mathbf{0}, \mathbf{I}) \quad (5)$$

4.4. Theoretical Analysis

In this section, we analyze the role of the variational regularization term through the lens of the information bottleneck principle (Tishby & Zaslavsky, 2015; Alemi et al., 2016).

We denote the complete input to the model as $X = (A_t, t, C)$ and the prediction target as $Y = A_0$. The model’s prediction process can be decomposed as follows: it first encodes the skip-connection features S and the filtered feature \hat{Z} , where $\hat{Z} \sim p_\theta(\cdot|X)$; it then decodes the prediction based on S and \hat{Z} , yielding $Y \sim q_\phi(\cdot|S, \hat{Z})$. Following Tishby & Zaslavsky (2015), we can formulate the following optimization objective:

$$\mathcal{L}_{\text{IB}} = I(\hat{Z}, S; Y) - \alpha I(\hat{Z}; X) \quad (6)$$

where $I(\cdot; \cdot)$ denotes mutual information, and $\alpha > 0$ is the regularization weight. Our goal is to maximize Eq. (6),

which encourages \hat{Z} and S to encode information that is useful for predicting Y , while forcing \hat{Z} to “forget” task-irrelevant information in X . However, directly computing mutual information in (6) is intractable. Alemi et al. (2016) propose to estimate it via variational inference by optimizing an evidence lower bound(ELBO), as stated in the following theorem:

Theorem 4.1 (Alemi et al. (2016)).

$$\begin{aligned} \mathcal{L}_{\text{IB}} &\geq \mathcal{L}_{\text{ELBO}} \\ &:= I_{\text{BA}}(\hat{Z}, S; Y) - \alpha R(\hat{Z}; X) \end{aligned} \quad (7)$$

Here, each component are defined as:

$$I_{\text{BA}}(\hat{Z}, S; Y) := \mathbb{E} \left[\log q_{\phi}(Y|\hat{Z}, S) \right] + H(Y) \quad (8)$$

$$R(\hat{Z}; X) := \mathbb{E} \left[\text{KL}(p_{\theta}(\hat{Z}|X)) \| q(\hat{Z}) \right] \quad (9)$$

where I_{BA} is known as the Barber–Agakov lower bound (Barber & Agakov, 2004).

Based on Theorem 4.1, we successfully reformulate Eq.(6) into a computable objective. Furthermore, under the framework described in Sec.4.3, we can show that $\mathcal{L}_{\text{policy}}$ and $-2\sigma^2 \mathcal{L}_{\text{ELBO}}$ differ only by a parameter-independent constant:

Corollary 4.2. *Let the decoder be a Gaussian distribution with fixed variance*

$$q_{\phi}(A_0|\hat{Z}, S) = \mathcal{N} \left(\hat{A}_0(\hat{Z}, S), \sigma^2 \mathbf{I} \right) \quad (10)$$

and let \hat{Z} be obtained as described in Sec.4.3. If we set $\alpha = \frac{\beta}{2\sigma^2}$, then:

$$\mathcal{L}_{\text{policy}} = -2\sigma^2 \mathcal{L}_{\text{ELBO}} + C \quad (11)$$

where C is a constant.

Corollary 4.2 clearly shows that minimizing Eq.(4) is equivalent to maximizing the ELBO in Eq.(7).Therefore, adding the variational regularization module is equivalent to optimizing Eq.(6), which theoretically guarantees its ability to perform “information filtering”. The detailed proof can be found in Appendix A.

5. Experiments

5.1. Experimental Setup

Simulation Environment. We evaluate our method on three widely used benchmarks: RoboTwin2.0 (Chen et al., 2025), Adroit (Rajeswaran et al., 2017), and MetaWorld (Yu et al., 2020). RoboTwin2.0 primarily focuses on dual-arm gripper manipulation, offering a diverse set of assets and task categories, and providing scripted policies to enable automated

data collection. Adroit focuses on dexterous hand manipulation with high-dimensional continuous control, serving as a challenging testbed for learning precise, long-horizon skills. MetaWorld offers a diverse suite of single-arm manipulation tasks, organized into multiple difficulty levels following prior work (Seo et al., 2023).

Training and Evaluation Metrics. For a fair comparison, we follow the official training and evaluation protocols for all benchmarks:

- For RoboTwin2.0, we train the model using 50 expert demonstrations as specified by the official guidelines, and evaluate each task on 100 randomly generated scenes with 100 different random seeds.
- For Adroit and MetaWorld, we follow DP3 (Ze et al., 2024) and use 10 expert demonstrations to assess the data efficiency of our method. We run three independent trials with random seeds 0, 1, 2. During training, we evaluate the policy every 200 epochs; each evaluation consists of 20 rollouts per task, from which we compute the success rate. For each seed, we track the success rate over training and define SR_5 as the average of the top five success rates. We report the average SR_5 across the three seeds.

Implementation Details. We train our VR based on DP3 on a single NVIDIA RTX 5880. All training and inference settings are kept identical to the official deployment(except for the additional KL weight term β). Following DP3 (Ze et al., 2024), we use a DDIM (Song et al., 2020a) noise scheduler with 100 diffusion steps during training and 10 steps at inference, and optimize with AdamW (Loshchilov & Hutter, 2017) using an initial learning rate of 1×10^{-4} and a cosine decay schedule. Both actions and robot states are normalized to $[-1, 1]$ to stabilize training. All models are trained for 3,000 epochs with a batch size of 256 on RoboTwin2.0 and 128 on Adroit and MetaWorld. For most tasks, setting the KL weight β to 1×10^{-9} yields sufficiently strong performance. For a small number of tasks, we tune the KL weight based on task characteristics to achieve better results. The detailed hyperparameter settings are provided in Appendix B.

5.2. Comparison with the State-of-the-art Methods

RoboTwin2.0. As shown in Tab. 1 and 3, we compare our method against the state-of-the-art approaches reported on the RoboTwin2.0 leaderboard¹ across 49 tasks. Tab. 1 indicates that augmenting DP3 with our VR module yields consistent performance gains on almost all tasks, with the largest improvement of 27 percentage points (on Open Microwave, from 61% to 88%). Notably, DP3+VR achieves

¹<https://robotwin-platform.github.io/leaderboard>

Table 1. Evaluation on the Robotwin2.0 benchmark. Each task is tested across 100 randomly generated scenes.

	Adjust Bottle	Beat Block Hammer	Blocks Ranking Size	Click Alarmclock	Click Bell	Dump Bin Bigbin	Grab Roller
DP	97.0	42.0	1.0	61.0	54.0	49.0	98.0
π_0	90.0	43.0	7.0	63.0	44.0	83.0	96.0
DP3	99.0	72.0	2.0	77.0	90.0	85.0	98.0
DP3 + VR (Ours)	100.0 (↑ 1)	88.0 (↑ 16)	5.0 (↑ 3)	90.0 (↑ 13)	100.0 (↑ 10)	92.0 (↑ 7)	99.0 (↑ 1)
	Handover Block	Handover Mic	Hanging Mug	Lift Pot	Move Can Pot	Move Pillbottle Pad	Move Playingcard Away
DP	10.0	53.0	8.0	39.0	39.0	1.0	47.0
π_0	45.0	98.0	11.0	84.0	58.0	21.0	53.0
DP3	70.0	100.0	17.0	97.0	70.0	41.0	68.0
DP3 + VR (Ours)	91.0 (↑ 21)	100.0 (0)	20.0 (↑ 3)	97.0 (0)	90.0 (↑ 20)	53.0 (↑ 12)	69.0 (↑ 1)
	Move Stapler Pad	Open Laptop	Open Microwave	Pick Diverse Bottles	Pick Dual Bottles	Place A2B Left	Place A2B Right
DP	1.0	49.0	5.0	6.0	24.0	2.0	13.0
π_0	0.0	85.0	80.0	27.0	57.0	31.0	27.0
DP3	12.0	82.0	61.0	52.0	60.0	46.0	49.0
DP3 + VR (Ours)	15.0 (↑ 3)	81.0 (↓ 1)	88.0 (↑ 27)	64.0 (↑ 12)	71.0 (↑ 11)	47.0 (↑ 1)	42.0 (↓ 7)
	Place Bread Basket	Place Bread Skillet	Place Burger Fries	Place Can Basket	Place Cans Plasticbox	Place Container Plate	Place Dual Shoes
DP	14.0	11.0	72.0	18.0	40.0	41.0	8.0
π_0	17.0	23.0	80.0	41.0	34.0	88.0	15.0
DP3	26.0	19.0	72.0	67.0	48.0	86.0	13.0
DP3 + VR (Ours)	37.0 (↑ 11)	25.0 (↑ 6)	76.0 (↑ 4)	78.0 (↑ 11)	70.0 (↑ 22)	86.0 (0)	17.0 (↑ 4)
	Place Empty Cup	Place Fan	Place Mouse Pad	Place Object Basket	Place Object Scale	Place Object Stand	Place Phone Stand
DP	37.0	3.0	0.0	15.0	1.0	22.0	13.0
π_0	37.0	20.0	7.0	16.0	10.0	36.0	35.0
DP3	65.0	36.0	4.0	65.0	15.0	60.0	44.0
DP3 + VR (Ours)	79.0 (↑ 14)	41.0 (↑ 5)	8.0 (↑ 4)	67.0 (↑ 2)	17.0 (↑ 2)	64.0 (↑ 4)	44.0 (0)
	Place Shoe	Press Stapler	Put Bottles Dustbin	Put Object Cabinet	Rotate QRcode	Scan Object	Shake Bottle Horizontally
DP	23.0	6.0	22.0	42.0	13.0	9.0	59.0
π_0	28.0	62.0	54.0	68.0	68.0	18.0	99.0
DP3	58.0	69.0	60.0	72.0	74.0	31.0	100.0
DP3 + VR (Ours)	56.0 (↓ 2)	74.0 (↑ 5)	65.0 (↑ 5)	67.0 (↓ 5)	72.0 (↓ 2)	33.0 (↑ 2)	100.0 (0)
	Shake Bottle	Stack Blocks Three	Stack Blocks Two	Stack Bowls Three	Stack Bowls Two	Stamp Seal	Turn Switch
DP	65.0	0.0	7.0	63.0	61.0	2.0	36.0
π_0	97.0	17.0	42.0	66.0	91.0	3.0	27.0
DP3	98.0	1.0	24.0	57.0	83.0	18.0	46.0
DP3 + VR (Ours)	99.0 (↑ 1)	6.0 (↑ 5)	36.0 (↑ 12)	64.0 (↑ 7)	87.0 (↑ 4)	36.0 (↑ 18)	54.0 (↑ 8)

Table 2. Evaluation on the Adroit and MetaWorld benchmark. Each task is trained and tested across 3 different seeds. Unavailable results are denoted by “-”.

Method	Adroit			MetaWorld					
	Hammer	Door	Pen	Assembly	Disassemble	Stick-Push	Reach-Wall	Stick-Pull	Pick-Place-Wall
BCRNN	0	0	9	3	32	45	—	—	—
IBC	0	0	9	0	1	16	—	—	—
DP	48	50	25	15	43	63	59	11	5
DP3*	100.0	62.0	43.7	99.6	75.0	100.0	70.7	74.3	82.7
DP3 + VR (Ours)	100.0 (0)	67.3 (↑ 5.3)	53.7 (↑ 10)	100.0 (↑ 0.4)	90.0 (↑ 15)	100.0 (0)	75.2 (↑ 4.5)	75.3 (↑ 1)	84.0 (↑ 1.3)

Table 3. Average success rate (%) across 49 Robotwin2.0 tasks.

Metric	DP	π_0	DP3	DP3 + VR (Ours)
Avg. (%)	28.6	47.0	56.3	62.4 (↑ 6.1)

Table 4. Average SR₅ across 9 Adroit and MetaWorld tasks.

Metric	DP	DP3	DP3 + VR (Ours)
Avg. (%)	35.4	78.7	82.8 (↑ 4.1)

improvements of at least 10 percentage points on nearly one-third of the tasks (15 out of 49). We further compute the average success rate over all 49 tasks for each method, as summarized in Tab. 3. Although the VR module introduces

virtually no additional parameters, it boosts the baseline (DP3) by 6.1 percentage points on average, reaching an overall success rate of 62.4%.

Results on Adroit and MetaWorld. As shown in Tab. 2 and 4, we evaluate the data efficiency of our method on Adroit and MetaWorld, using only 10 expert demonstrations for training. Even under this low-data regime, VR consistently improves DP3 across multiple tasks, yielding an average SR₅ gain of 4.1 percentage points over the baseline.

5.3. VR Improves the SNR of Backbone Feature

We further use the same random masking protocol to examine whether VR indeed improves the signal-to-noise ratio of the backbone features. As indicated by the green curves in Fig. 3a–3h, VR can reverse the effect of masking the

entire backbone: what previously led to a performance gain now causes a performance drop. This suggests that VR suppresses noisy components, making the features contain more useful signal. While the peak performance under masking after adding VR may still exceed the unmasked baseline—implying that some noise may remain—the peak gain becomes clearly smaller, further indicating that VR reduces the overall noise level in the backbone features.

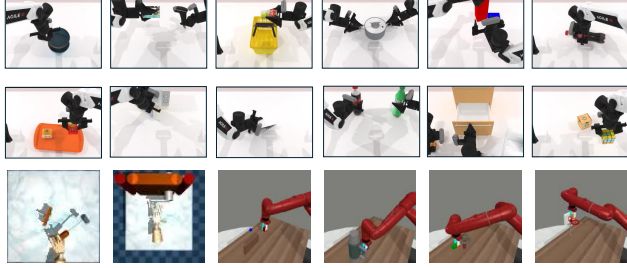


Figure 4. Simulation experiments visualization samples across RoboTwin2.0, Adroit and MetaWorld benchmarks. Our method consistently improves the baseline model across a wide range of tasks on multiple benchmarks.

5.4. Ablation Studies

We conduct ablation studies on four tasks: Adroit-Door, Adroit-Pen, MetaWorld-Disassemble, and MetaWorld-StickPull. These tasks cover both high-dimensional and low-dimensional control settings, and we use only 10 demonstrations for each task. The results are summarized in Tab. 5 and Fig. 5.

Necessity of Diffusion Timesteps in VR. As shown in Tab. 5, w/o t denotes the variant that does not inject diffusion-timestep information into the VR module. We observe that it can still improve over the baseline($\uparrow 2.63$); however, injecting t leads to a substantial additional gain($\uparrow 7.83$). This suggests that the noise embedded in backbone features may vary across different diffusion timesteps, and thus explicitly providing timestep information helps the module better disentangle noise from the features.

Impact of Different KL Weights. The KL Weight β controls the strength of information filtering: larger values correspond to stronger regularization, allowing less information to pass through. We conduct an ablation study on the effect of β , and the results are shown in Fig. 5. We observe that different tasks peak at different ranges of β ; nevertheless, setting $\beta = 1e-9$ consistently improves performance across most tasks.

Table 5. Necessity of Diffusion Timesteps in VR.

Method	Door	Pen	Disassemble	StickPull	Average
DP3	62.0	43.7	75.0	74.3	63.75
DP3+VR w/o t	64.0	43.8	87.7	70.0	66.38
DP3+VR	67.3	53.7	90.0	75.3	71.58

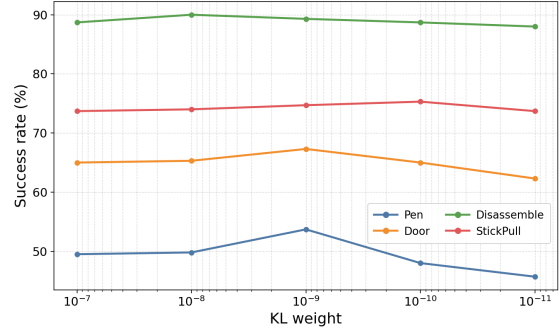


Figure 5. Impact of Different KL Weights (β)



Figure 6. Real-world Experiments. The image sequence illustrates the robot successfully grasping and stacking the cups, demonstrating the robustness of our method on real-world robotic manipulation tasks.

5.5. Real-World Experiments

We further evaluate the effectiveness of our method in a real-world cup-stacking experiment. As illustrated in Fig. 6, the robot must precisely grasp a cup and stack it on top of another cup. We conduct 15 trials and record the success rate; the results are reported in Tab. 6. As can be seen, incorporating VR improves DP3’s success rate by 13.4%, indicating that our method remains effective in the real world and is practical for real-world deployment. See Appendix B.2 for detailed experimental settings.

Table 6. Real-world Experiments Success Rate.

Metric	DP3	DP3+VR (Ours)
SR (%)	73.3	86.7 ($\uparrow 13.4$)

6. Conclusions

In this paper, we study how to adaptively filter redundant and noisy information from the backbone features in the decoder of diffusion-based policies. We first apply random masking to intermediate features in the U-Net decoder, suggesting that these backbone features may contain task-irrelevant noise. Building on this observation, we propose **Variational Regularization (VR)**, a simple but effective approach that adaptively suppresses noise while preserving the most task-relevant information. Extensive simulation results demonstrate that VR consistently improves performance across a wide range of tasks. Real-world experiments further validate its effectiveness.

Impact Statement

This paper presents work whose goal is to advance the field of Machine Learning. There are many potential societal consequences of our work, none which we feel must be specifically highlighted here.

References

Achille, A. and Soatto, S. Information dropout: Learning optimal representations through noisy computation. *IEEE transactions on pattern analysis and machine intelligence*, 40(12):2897–2905, 2018.

Alemi, A. A., Fischer, I., Dillon, J. V., and Murphy, K. Deep variational information bottleneck. *arXiv preprint arXiv:1612.00410*, 2016.

Argall, B. D., Chernova, S., Veloso, M., and Browning, B. A survey of robot learning from demonstration. *Robotics and autonomous systems*, 57(5):469–483, 2009.

Bai, S., Zhou, W., Ding, P., Zhao, W., Wang, D., and Chen, B. Rethinking latent redundancy in behavior cloning: An information bottleneck approach for robot manipulation. *arXiv preprint arXiv:2502.02853*, 2025.

Barber, D. and Agakov, F. The im algorithm: a variational approach to information maximization. *Advances in neural information processing systems*, 16(320):201, 2004.

Cao, J., Zhang, Q., Sun, J., Wang, J., Cheng, H., Li, Y., Ma, J., Wu, K., Xu, Z., Shao, Y., et al. Mamba policy: Towards efficient 3d diffusion policy with hybrid selective state models. *arXiv preprint arXiv:2409.07163*, 2024.

Chalk, M., Marre, O., and Tkacik, G. Relevant sparse codes with variational information bottleneck. *Advances in Neural Information Processing Systems*, 29, 2016.

Chen, T., Chen, Z., Chen, B., Cai, Z., Liu, Y., Li, Z., Liang, Q., Lin, X., Ge, Y., Gu, Z., et al. Robotwin 2.0: A scalable data generator and benchmark with strong domain randomization for robust bimanual robotic manipulation. *arXiv preprint arXiv:2506.18088*, 2025.

Chi, C., Xu, Z., Feng, S., Cousineau, E., Du, Y., Burchfiel, B., Tedrake, R., and Song, S. Diffusion policy: Visuomotor policy learning via action diffusion. *arXiv preprint arXiv:2303.04137*, 2023.

Dhariwal, P. and Nichol, A. Diffusion models beat gans on image synthesis. *Advances in neural information processing systems*, 34:8780–8794, 2021.

Ho, J., Jain, A., and Abbeel, P. Denoising diffusion probabilistic models. *Advances in Neural Information Processing Systems*, 33:6840–6851, 2020.

Kingma, D. P. and Welling, M. Auto-encoding variational bayes. *arXiv preprint arXiv:1312.6114*, 2013.

Li, J., Monroe, W., and Jurafsky, D. Understanding neural networks through representation erasure. *arXiv preprint arXiv:1612.08220*, 2016.

Liu, S., Wu, L., Li, B., Tan, H., Chen, H., Wang, Z., Xu, K., Su, H., and Zhu, J. Rdt-1b: a diffusion foundation model for bimanual manipulation. *arXiv preprint arXiv:2410.07864*, 2024.

Loshchilov, I. and Hutter, F. Decoupled weight decay regularization. *arXiv preprint arXiv:1711.05101*, 2017.

Nichol, A. Q. and Dhariwal, P. Improved denoising diffusion probabilistic models. In *International conference on machine learning*, pp. 8162–8171. PMLR, 2021.

Oktay, O., Schlemper, J., Folgoc, L. L., Lee, M., Heinrich, M., Misawa, K., Mori, K., McDonagh, S., Hammerla, N. Y., Kainz, B., et al. Attention u-net: Learning where to look for the pancreas. *arXiv preprint arXiv:1804.03999*, 2018.

Osa, T., Pajarinen, J., Neumann, G., Bagnell, J. A., Abbeel, P., and Peters, J. An algorithmic perspective on imitation learning. *Foundations and Trends® in Robotics*, 7(1-2): 1–179, 2018.

Perez, E., Strub, F., De Vries, H., Dumoulin, V., and Courville, A. Film: Visual reasoning with a general conditioning layer. In *Proceedings of the AAAI conference on artificial intelligence*, volume 32, 2018.

Prasad, A., Lin, K., Wu, J., Zhou, L., and Bohg, J. Consistency policy: Accelerated visuomotor policies via consistency distillation. *arXiv preprint arXiv:2405.07503*, 2024.

Rajeswaran, A., Kumar, V., Gupta, A., Vezzani, G., Schulman, J., Todorov, E., and Levine, S. Learning complex dexterous manipulation with deep reinforcement learning and demonstrations. *arXiv preprint arXiv:1709.10087*, 2017.

Ramesh, A., Dhariwal, P., Nichol, A., Chu, C., and Chen, M. Hierarchical text-conditional image generation with clip latents. *arXiv preprint arXiv:2204.06125*, 1(2):3, 2022.

Rombach, R., Blattmann, A., Lorenz, D., Esser, P., and Ommer, B. High-resolution image synthesis with latent diffusion models. In *Proceedings of the IEEE/CVF Conference on Computer Vision and Pattern Recognition*, pp. 10684–10695, 2022.

Ronneberger, O., Fischer, P., and Brox, T. U-net: Convolutional networks for biomedical image segmentation. In *International Conference on Medical image computing and*

computer-assisted intervention, pp. 234–241. Springer, 2015.

Ross, S., Gordon, G., and Bagnell, D. A reduction of imitation learning and structured prediction to no-regret online learning. In *Proceedings of the fourteenth international conference on artificial intelligence and statistics*, pp. 627–635. JMLR Workshop and Conference Proceedings, 2011.

Seo, Y., Hafner, D., Liu, H., Liu, F., James, S., Lee, K., and Abbeel, P. Masked world models for visual control. In *Conference on Robot Learning*, pp. 1332–1344. PMLR, 2023.

Si, C., Huang, Z., Jiang, Y., and Liu, Z. Freeu: Free lunch in diffusion u-net. In *Proceedings of the IEEE/CVF Conference on Computer Vision and Pattern Recognition*, pp. 4733–4743, 2024.

Song, J., Meng, C., and Ermon, S. Denoising diffusion implicit models. *arXiv preprint arXiv:2010.02502*, 2020a.

Song, Y., Sohl-Dickstein, J., Kingma, D. P., Kumar, A., Ermon, S., and Poole, B. Score-based generative modeling through stochastic differential equations. *arXiv preprint arXiv:2011.13456*, 2020b.

Tishby, N. and Zaslavsky, N. Deep learning and the information bottleneck principle. In *2015 ieee information theory workshop (itw)*, pp. 1–5. Ieee, 2015.

Wang, Z., Li, Z., Mandlekar, A., Xu, Z., Fan, J., Narang, Y., Fan, L., Zhu, Y., Balaji, Y., Zhou, M., et al. One-step diffusion policy: Fast visuomotor policies via diffusion distillation. *arXiv preprint arXiv:2410.21257*, 2024.

Xia, W., Zhang, J., Zhang, C., Wang, Y., Gong, Y., and Mei, J. Iss policy : Scalable diffusion policy with implicit scene supervision. *arXiv preprint arXiv:2512.15020*, 2025.

Xian, Z., Gkanatsios, N., Gervet, T., Ke, T.-W., and Fragkiadaki, K. Chaineddiffuser: Unifying trajectory diffusion and keypose prediction for robotic manipulation. In *7th Annual Conference on Robot Learning*, 2023.

Yan, S., Zhang, Z., Han, M., Wang, Z., Xie, Q., Li, Z., Li, Z., Liu, H., Wang, X., and Zhu, S.-C. M 2 diffuser: Diffusion-based trajectory optimization for mobile manipulation in 3d scenes. *IEEE Transactions on Pattern Analysis and Machine Intelligence*, 2025.

Yu, T., Quillen, D., He, Z., Julian, R., Hausman, K., Finn, C., and Levine, S. Meta-world: A benchmark and evaluation for multi-task and meta reinforcement learning. In *Conference on robot learning*, pp. 1094–1100. PMLR, 2020.

Ze, Y., Zhang, G., Zhang, K., Hu, C., Wang, M., and Xu, H. 3d diffusion policy: Generalizable visuomotor policy learning via simple 3d representations. *arXiv preprint arXiv:2403.03954*, 2024.

Zhang, Q., Liu, Z., Fan, H., Liu, G., Zeng, B., and Liu, S. Flowpolicy: Enabling fast and robust 3d flow-based policy via consistency flow matching for robot manipulation. In *Proceedings of the AAAI Conference on Artificial Intelligence*, volume 39, pp. 14754–14762, 2025.

A. Proof of Theorem 4.1 and Corollary 4.2

A.1. Proof of Theorem 4.1

Proof. We first consider the first term $I(\hat{Z}, S; Y)$ in Eq.(6). By the definition of differential entropy $H(Y) = \mathbb{E}[-\log q(Y)]$, we have:

$$I(\hat{Z}, S; Y) = \mathbb{E}_{(\hat{Z}, S), Y} \left[\log \frac{q_\phi(Y|\hat{Z}, S)}{q(Y)} \right] \quad (12)$$

$$= \mathbb{E}_{(\hat{Z}, S), Y} \left[\log q_\phi(Y|\hat{Z}, S) \right] - \mathbb{E}_Y [\log q(Y)] \quad (13)$$

$$= \mathbb{E} \left[\log q_\phi(Y|\hat{Z}, S) \right] + H(Y) \quad (14)$$

Next, we consider the second regularization term $I(\hat{Z}; X)$. Using variational inference, we obtain:

$$I(\hat{Z}; X) = \mathbb{E}_{X, \hat{Z}} \left[\log \frac{p_\theta(\hat{Z}|X)}{p_\theta(\hat{Z})} \right] \quad (15)$$

$$= \mathbb{E}_{X, \hat{Z}} \left[\log \left(\frac{p_\theta(\hat{Z}|X)}{q(\hat{Z})} \frac{q(\hat{Z})}{p_\theta(\hat{Z})} \right) \right] \quad (16)$$

$$= \mathbb{E}_{X, \hat{Z}} \left[\log \frac{p_\theta(\hat{Z}|X)}{q(\hat{Z})} \right] - \mathbb{E}_{\hat{Z}} \left[\log \frac{p_\theta(\hat{Z})}{q(\hat{Z})} \right] \quad (17)$$

$$= \iint p(X) p_\theta(\hat{Z}|X) \log \frac{p_\theta(\hat{Z}|X)}{q(\hat{Z})} d\hat{Z} dX - \text{KL}(p_\theta(\hat{Z})\|q(\hat{Z})) \quad (18)$$

$$\geq \mathbb{E} \left[\text{KL}(p_\theta(\hat{Z}|X)\|q(\hat{Z})) \right] \quad (19)$$

where $q(\hat{Z})$ is the standard normal distribution. Combining Eqs.(14) and (19), we obtain:

$$\mathcal{L}_{\text{IB}} = I(\hat{Z}, S; Y) - \alpha I(\hat{Z}; X) \quad (20)$$

$$\geq \mathbb{E} \left[\log q_\phi(Y|\hat{Z}, S) \right] + H(Y) - \alpha \mathbb{E} \left[\text{KL}(p_\theta(\hat{Z}|X)\|q(\hat{Z})) \right] \quad (21)$$

$$:= I_{\text{BA}}(\hat{Z}, S; Y) - \alpha R(\hat{Z}; X) \quad (22)$$

$$:= \mathcal{L}_{\text{ELBO}} \quad (23)$$

□

A.2. Proof of Corollary 4.2

Proof. In our model, \hat{Z} is determined by Z and t , and both Z and t are derived from the input X . Therefore, we can rewrite $p_\theta(\hat{Z} | X)$ as $p_\theta(\hat{Z} | X) = p_\theta(\hat{Z} | Z, t)$. Furthermore, since $q_\phi(A_0|\hat{Z}, S) = \mathcal{N}(\hat{A}_0(\hat{Z}, S), \sigma^2 \mathbf{I})$, the Barber–Agakov lower bound I_{BA} can be computed as:

$$I_{\text{BA}}(\hat{Z}, S; A_0) = \mathbb{E} \left[\log q_\phi(A_0|\hat{Z}, S) \right] + H(A_0) \quad (24)$$

$$= \mathbb{E} \left[-\frac{\|\hat{A}_0 - A_0\|^2}{2\sigma^2} \right] + H(A_0) \quad (25)$$

Therefore, $\mathcal{L}_{\text{ELBO}}$ can be rewritten as:

$$\mathcal{L}_{\text{ELBO}} = \mathbb{E} \left[\log q_\phi(A_0 | \hat{Z}, S) \right] + H(A_0) - \alpha \mathbb{E} \left[\text{KL}(p_\theta(\hat{Z} | X) \| q(\hat{Z})) \right] \quad (26)$$

$$= \mathbb{E} \left[-\frac{\|\hat{A}_0 - A_0\|^2}{2\sigma^2} \right] + H(A_0) - \alpha \mathbb{E} \left[\text{KL}(p_\theta(\hat{Z} | Z, t) \| q(\hat{Z})) \right] \quad (27)$$

$$= -\frac{1}{2\sigma^2} \mathbb{E} \left[\|\hat{A}_0 - A_0\|^2 + \beta \text{KL}(p_\theta(\hat{Z} | Z, t) \| q(\hat{Z})) \right] + H(A_0) \quad (28)$$

$$= -\frac{1}{2\sigma^2} \mathcal{L}_{\text{policy}} + H(A_0) \quad (29)$$

Since $H(A_0)$ is independent of the model parameters, it can be treated as a constant, and thus:

$$\mathcal{L}_{\text{policy}} = -2\sigma^2 \mathcal{L}_{\text{ELBO}} + C \quad (30)$$

□

B. Implementation Details

B.1. Training and Evaluation

In this section, we provide the essential hyperparameters required to reproduce our results. Overall, except for the newly introduced KL weight β , all other training and inference settings follow the default configurations of the benchmark and the baseline to ensure a fair comparison. Detailed hyperparameter choices are listed in Tab. 7, and the task-specific KL weights β are reported in Tab. 8.

Table 7. Detailed Hyperparameter Settings

Type	Parameter	Value
Training	batch size(Robotwin2.0)	256
	batch size(Adroit&MetaWorld)	128
	num epochs	3000
	optimizer	AdamW
	weight decay	$1e - 6$
	lr scheduler	cosine
	lr warmup steps	500
	learning rate	$1e - 4$
	horizon(Robotwin2.0)	8
	horizon(Adroit&MetaWorld)	16
	num. action steps(Robotwin2.0)	6
	num. action steps(Adroit&MetaWorld)	8
	observation steps(Robotwin2.0)	3
	observation steps(Adroit&MetaWorld)	2
	encoder output dim.(Robotwin2.0)	128
	encoder output dim.(Adroit&MetaWorld)	64
Inference	num. inference steps	10
	num. train steps	100

B.2. Real-World Experiments

We validate the effectiveness of our method on an AgileX Piper robot. Real-world visual observations are captured using a single Intel RealSense D455 camera, and the model is deployed for on-robot action inference on an NVIDIA RTX 4060 GPU. Our real-world setup and task procedure are shown in Fig. 7. We collect real-world expert demonstrations via teleoperation, obtaining 50 trajectories for training.

Table 8. KL weights β for each task.

Benchmark	Task	Value
RoboTwin2.0	Handover Mic	$5e - 9$
	Move Stapler Pad	$5e - 9$
	Place Phone Stand	$1e - 8$
	Place Shoe	$5e - 10$
	Put Object Cabinet	$5e - 10$
	Rotate QRcode	$5e - 10$
	Scan Object	$5e - 9$
	Turn Switch	$5e - 9$
	All Others	$1e - 9$
Adroit&MetaWorld	MetaWorld-ReachWall	$1e - 10$
	All Others	$1e - 9$



Figure 7. Real-World Experiment Setup.